THE UNIVERSITY *of* EDINBURGH

Edinburgh Research Explorer

Dubiofossils from a Mars-analogue subsurface palaeoenvironment: the limits of biogenicity criteria

OPEN ACCESS

Dubiofossils from a Mars-analogue subsurface palaeoenvironment: the limits of biogenicity criteria

Sean McMahon[1,2], Magnus Ivarsson[3,4], David Wacey[5], Martin Saunders[5], Veneta Belivanova[4], David Muirhead[6], Pamela Knoll[7], Oliver Steinbock[7], Daniel Frost[8]

1. UK Centre for Astrobiology, School of Physics and Astronomy, University of Edinburgh, James Clerk Maxwell Building, Peter Guthrie Tait Road, Edinburgh EH9 3FD, UK. Email: **sean.mcmahon@ed.ac.uk**
2. School of GeoSciences, University of Edinburgh, Grant Institute, James Hutton Road, EH9 3FE, UK.
3. Department of Biology, University of Southern Denmark, DK-5230, Odense, Denmark
4. Swedish Museum of Natural History, SE-104 05 Stockholm, Sweden
5. Centre for Microscopy Characterisation and Analysis, The University of Western Australia, 35 Stirling Highway, Perth, WA 6009, Australia
6. School of Geosciences, University of Aberdeen, King's College, Aberdeen, AB24 3UE, U.K.
7. Department of Chemistry and Biochemistry, Florida State University, Tallahassee, FL 32306, USA
8. Department of Earth & Planetary Science, University of California, Berkeley, CA 94720, USA

Key words: Dubiofossil, pseudofossil, biogenicity, deep biosphere, Mars, serpentinization

Abstract

The search for a fossil record of Earth's deep biosphere, partly motivated by potential analogies with subsurface habitats on Mars, has uncovered numerous assemblages of inorganic microfilaments and tubules inside ancient pores and fractures. Although these enigmatic objects are morphologically similar to mineralized microorganisms (and some contain organic carbon), they also resemble some abiotic structures. Palaeobiologists have responded to this ambiguity by evaluating problematic filaments against checklists of "biogenicity criteria". Here, we describe material that tests the limits of this approach. We sampled Jurassic calcite veins formed through

subseafloor serpentinization, a water–rock reaction that can fuel the deep biosphere and is known to have occurred widely on Mars. At two localities ~4 km apart, veins contained curving, branched microfilaments composed of Mg-silicate and Fe-oxide minerals. Using a wide range of analytical techniques including synchrotron X-ray microtomography and scanning transmission electron microscopy, we show that these features meet many published criteria for biogenicity and are comparable to fossilized cryptoendolithic fungi or bacteria. However, we argue that abiotic processes driven by serpentinization could account for the same set of lifelike features, and report a chemical garden experiment that supports this view. These filaments are therefore most objectively described as dubiofossils, a designation we here defend from criticism and recommend over alternative approaches, but which nevertheless signifies an impasse. Similar impasses can be anticipated in the future exploration of subsurface palaeo-habitats on Earth and Mars. To avoid them, further studies are required in biomimetic geochemical self-organization, microbial taphonomy and micro-analytical techniques, with a focus on subsurface habitats.

Introduction

Microbial communities in deep fractured bedrock on Earth serve as model systems in the search for life on Mars, where habitable conditions may be restricted to the subsurface (e.g., Stevens and McKinley, 1995). We will not be able to sample any extant deep biosphere on Mars in the near future, but the fossil remains of an ancient deep biosphere might now be exposed at the surface. On Earth, however, the fossil record of rock-hosted (i.e., "endolithic") subsurface habitats is sparsely sampled and poorly understood. Investigations of ancient, mineral-filled and unfilled fractures and voids have provided few unambiguous fossils, but yielded numerous

examples of µm–mm-thick filaments composed of Fe- and Mg-(oxyhydr)oxides and/or clay minerals (reviewed by McMahon and Ivarsson, 2019 and by Ivarsson et al., 2020). Although they commonly lack organic matter, the morphological, textural and compositional characteristics of these filaments are usually found to meet established "biogenicity criteria" for discriminating true fossils from pseudofossils. They have accordingly been interpreted as fossils and recommended as important analogues in the search for fossils on Mars (e.g., Hofmann and Farmer, 2000, Hofmann et al., 2008; Onstott et al. 2019).

Specific biogenicity criteria applicable to fossilized fracture-dwelling (chasmoendolithic) and cavity-dwelling (cryptoendolithic) filamentous organisms were listed by McLoughlin et al. (2010). The additional criteria outlined by Johannessen et al. (2020) for recognising fossil Fe-oxidizing filamentous bacteria in hydrothermal cherts may also be relevant in these settings. However, it was recently shown that Fe-oxyhydroxide tubules produced in simple, abiotic chemical gardens meet many published biogenicity criteria; e.g., they possess circular cross-sections; curving, branching growth trajectories, and swellings (McMahon, 2019; cf. McLoughlin et al., 2010). In general, there are good reasons to doubt that "biogenicity criteria" can be reliably formulated on our present state of knowledge about the formation of lifelike microstructures in geochemical systems; more work in this area is needed to facilitate life-detection in the rock records of early Earth and Mars (Garcia-Ruiz et al., 2002; McMahon, 2019; Rouillard et al., 2021).

Despite these doubts, some reports of fossil assemblages from the deep biosphere are supported by organic geochemical evidence that is difficult to discount (Ivarsson et al., 2012; Ivarsson et

al., 2020). One particularly compelling example—a population of organically preserved archaeal colonies containing biomarker lipids—was recently reported from Cretaceous calcite–brucite veins in drill core extracted from the Iberia Margin (Klein et al., 2015). These fossils were localised to the gradational contact between two rock types, serpentinite and overlying ophicalcite, representing a redox boundary beneath the palaeo-seafloor. Serpentinite results from the hydrolysis and hydration of Fe- and Mg-silicate minerals in mafic and ultramafic rocks ("serpentinization"), while ophicalcite is a strongly oxidized, pervasively calcite-veined alteration product of serpentinite, which forms when serpentinite is fractured and carbonated by seawater mixing with the strongly alkaline fluids generated by serpentinization (Schwarzenbach et al., 2012). This water–rock reaction generates important electron donors for the deep biosphere (H_2 and CH_4) while also fracturing the rock and driving the precipitation of pore- and fracture-filling minerals, notably carbonates (Stevens and McKinley, 1995; McKinley et al., 2000; Kelley et al., 2005; Klein and McCollom, 2013). Serpentinization thus enhances both habitability and the potential for fossil preservation in fractured mafic and ultramafic rocks. The discovery of fossils in serpentinization–associated carbonates is of particular astrobiological interest because serpentinization is known to have occurred in some places on Mars, producing serpentine and carbonates detectable from orbit and in meteorites (e.g., Ehlmann et al. 2010; Changela and Bridges, 2010; Blamey et al., 2015). It may continue today, perhaps contributing to sporadic emissions of CH_4 from the martian surface/subsurface to the atmosphere (Krasnopolsky et al., 1997; Mumma et al., 2009; Fonti & Marzo, 2010; Webster et al., 2015; Giuranna et al., 2019).

Here, we report the results of a search for fossils in calcite veins from a Jurassic subseafloor serpentinizing system now exposed subaerially in Liguria, NW Italy. Our sampling strategy focused on the gradational serpentinite–ophicalcite contact, which in Liguria is geochemically and structurally analogous to the younger Iberia Margin material in which Klein et al. (2015) found fossiliferous veins (e.g., Schwarzenbach et al., 2012, 2013). Veins in our samples did not apparently contain organically preserved fossils, but did contain metalliferous mineral filaments (and other microstructures) similar to those previously reported from other ancient fractures and pore spaces (Milliken, 2001; Ivarsson et al., 2008; 2011; 2012; 2013).

Materials and Methods

Sample localities and acquisition

Samples were collected inland from the coastal towns of Deiva Marina and Bonassola in Eastern Liguria, NW Italy (**Fig 1**). The "classic" ophiolite sequence exposed in this region represents the oceanic lithosphere of the Ligurian-Piedmont Ocean, a western segment of the Tethys Ocean, which opened in the Jurassic as a consequence of left-lateral shear between the African and European plates (Bortolotti et al., 2001). At some point in the Jurassic, faulting and unroofing of the oceanic basement allowed seawater to percolate through upper mantle rocks (lherzolitic peridotite), generating the basal unit of the ophiolite sequence, a green-and-black serpentinite of undetermined thickness. Dykes cross-cutting these altered mantle rocks have been dated at 165 million years old (Bigazzi et al., 1972). The serpentinite is locally overlain by an ophicalcite unit known as the "Rosso Levanto", comprising maroon and violet oxidised serpentinite pervasively veined with calcite and variably brecciated (hence, the unit is often called the "Levanto

breccia"). Much of this breccia is thought to have been exposed directly at the seafloor; it contains some micritic sediment and at the top grades into a sedimentary breccia (the "Framura Breccia"; Treves and Harper, 1994). The ophiolite sequence is capped with a Jurassic–Palaeocene sedimentary succession that shows a shallowing-upward trend recording the convergence and closure of the ocean basin. The sequence was fully emplaced onto the continental crust by the middle Eocene (Bortolotti et al., 2001).

Calcite veins were sampled from gradational contacts between serpentinite and ophicalcite exposed in and around road cuts. As such, samples represent the lowermost reaches of the ophicalcite unit and probably formed at least tens of metres beneath the palaeo-seafloor. The samples described in the present study were found at two localities from which calcite–brucite veins were sampled and thin sectioned (**Fig 1**). At "Locality 1", material was sampled from a ~m-wide, heavily veined float block of serpentinite + ophicalcite at the base of a cliff at 44°11'51"N 9°35'25"E, near the town of Bonassola. This locality is within a hundred metres laterally of the Cava Galli quarry, in whose walls the gradational contact between serpentinite and ophicalcite spans a vertical thickness of 30 metres (Schwarzenbach et al., 2013). At "Locality 2", material was collected from a similar float piece at 44°13'51"N 9°32'60"E, near the town of Deiva Marina, about 4 km from the first sample and just outside the perimeter of the Cava La Sfinge quarry.

Optical and petrographic microscopy

Double-polished, uncoated petrographic thin sections of 150 μm thickness (unless otherwise stated) were prepared at the Open University Thin Sectioning Laboratory, Milton Keynes.

Optical microscopy was undertaken with a Leica DMLP Reflected/transmitted light polarizing microscope with DFC 420C camera and Leica Application Suite v 4.00, which was also used to measure the diameters of metalliferous filaments. Only filaments with well-defined, non-diffuse boundaries were measured.

Fluid inclusion paleothermometry

Fluid inclusion studies were performed on doubly polished wafers using a Linkam THMS-600 heating–freezing stage mounted on a Nikon Labophot transmission light microscope. The instrument, equipped with a range of objective lenses including a 100Å~ lens, was calibrated against synthetic H_2O (374.1 and 0.0°C) and CO_2 (−56.6°C) standards (Synthetic Fluid Inclusion Reference Set, Bubbles Inc., USA). The petrography of fluid inclusion assemblages was first examined at low magnifications using a NIKON Eclipse E600 microscope equipped with both transmitted white and incident ultraviolet light (UV) sources. Ultraviolet light, with an excitation wavelength of 365 nm, was provided by a high-pressure mercury lamp with a 420 nm barrier epi-fluorescence filter that allows only the long-wavelength UV to reach the sample.

Raman spectrometry

Two Raman instruments were used to investigate sample compositions, and more particularly to determine whether "D" and "G" bands attributable to disordered carbonaceous material could be measured. A Renishaw inVia Raman microscope at the University of Edinburgh was used to acquire Raman spectra from uncoated thin sections. The 514 nm, 2 mW laser beam was focused onto the samples using a 100× objective lens, providing an excitation spot of about 2 μm diameter. Raman point spectra were taken at different positions on the samples over the range

100–3200 cm-1. The spectra were acquired with a 30 s exposure time at 100% laser power. Renishaw Wire 2.0 software was used for data acquisition. Additionally, Raman mapping was performed on a *WITec alpha 300RA+* instrument with a *Toptica Photonics Xtra II* 785 nm laser source at the Centre for Microscopy, Characterisation and Analysis (CMCA) at the University of Western Australia (UWA). The laser was focused through a 100x/0.9 objective to obtain a spot size of <1 μm. Maps were acquired with the spectral centre of the detector adjusted to 944 cm^{-1}, with a motorised stage allowing XYZ displacement with precision of better than 1 μm. Spectral decomposition and subsequent image processing were performed using WITec Project FOUR software, with baseline subtraction using a 3rd or 4th order polynomial. Hematite maps were created by integrating over the ~290 cm^{-1} hematite Raman band. All analyses were conducted on material embedded below the surface of the thin section to avoid artefacts in the Raman spectra resulting from polishing and/or surface contamination.

Scanning electron microscopy

Scanning electron microscopy (SEM) and energy dispersive X-ray spectroscopy (EDS) of carbon-coated polished, uncovered thin sections were undertaken at the University of Glasgow using a Zeiss Sigma analytical SEM equipped with an Oxford Instruments X-Max silicon drift energy dispersive X-ray detector and an operating voltage of 20 kV.

Focused ion-beam milling and transmission electron microscopy, elemental mapping and electron diffractometry

TEM samples were prepared using a *FEI Helios Nanolab G3 CX* dual beam (FIB-SEM) instrument in the CMCA at UWA. Electron beam imaging was used to identify microstructures

of interest in the polished thin sections coated with c. 10 nm of gold, allowing site-specific TEM samples to be prepared. The TEM sections were prepared using a slightly modified version of the protocol for microstructure extraction given in Wacey *et al*. (2012), with milling and imaging parameters optimised to suit the specific type of sample (i.e., calcium carbonate matrix). Briefly, regions of interest (ROI) were covered with a protective (c. 2 μm-thick) platinum layer. Initial large trenches were milled either side of the ROI with a 21 nA Ga+ ion beam, and the trench faces cleaned up using a 9.3 nA beam. Element mapping within the FIB-SEM using energy-dispersive X-ray spectroscopy (EDS) was performed on some cleaned trench faces to gain a preliminary understanding of the chemistry of the filaments and their surrounding matrix. SEM-BSE imaging was also performed on cleaned trench faces during the thinning process. On reaching a thickness of c. 1.5-2 μm the ROI was extracted using an *in situ* micromanipulator, and attached to a *Pelco* copper TEM grid by welded platinum strips. This welding protocol means that there is no carbon film underneath the wafer that could potentially interfere with carbon elemental mapping in the TEM. Subsequent thinning of the ROI was performed with decreasing ion beam currents (0.79 nA then 0.23 nA). Final thinning was performed at lower voltage (16 kV and 1.3 nA current) followed by face cleaning at 5 kV and 15 pA. Average final wafer thicknesses were in the range of 150-200 nm.

TEM and STEM (scanning transmission electron microscopy) data were obtained using an *FEI Titan G2 80-200* TEM/STEM with *ChemiSTEM* technology operating at 200 kV equipped with a *Gatan SC1000* camera located in the CMCA at UWA. Crystal orientation and mass/density difference data were gained from high angle annular dark-field (HAADF) and bright field (BF) STEM imaging. Energy-dispersive X-ray spectroscopy (EDX) via the *ChemiSTEM* system

provided elemental maps and spectra. Lattice spacings of crystals to help determine mineralogy were obtained via selected area electron diffraction (SAED) using an aperture that selected a 600 nm field of view.

Synchrotron-radiation X-ray tomographic microscopy (SRXTM)

Synchrotron-radiation X-ray tomographic microscopy (SRXTM) was carried out at the X02DA TOMCAT beamline at the Swiss Light Source, Paul Scherrer Institut, Villigen, Switzerland. The sample selected for analysis was sawed from a thin section to proper size of about 3x3 mm square. A LuAG:Ce 20 um scintillator was used during the scanning process. For optimal penetration the energy of 28 keV was applied. A total of 1501 projections were acquired, during rotation of the specimen over 180°, post-processed and rearranged into flat- and darkfield-corrected sinograms. Exposure time per single projection was 1900 ms. Tomographic reconstruction was performed using a highly optimized algorithm based on the Fourier method (Marone and Stampanoni 2012), and the obtained tomographic volumes were visualized using Avizo 9.5.0 (FEI Company). With the 40× lens used, the resulting voxel size was 0.1625 μm.

Chemical garden experiments and analyses

A soluble polymetallic sulfate mineral (a member of the copiapite family) was obtained from the efflorescent deposits formed by pyrite oxidation associated with acid mine drainage at Baia Sprie, Romania (Buzatu et al., 2016). A small (0.096 g) sample of this mineral was dissolved in a beaker containing 20 ml of 0.9 M Na_2SiO_3(aq) at room temperature. Chemical gardens formed in minutes after the addition of the mineral. These were sampled and sputter-coated with a 20 nm layer of iridium. The coated samples were imaged using a FEI Nova 400 field emission scanning electron microscope (SEM) with an accelerating voltage between 10–15 kV. All compositional analyses were performed by energy dispersive X-ray (EDX) spectroscopy using an Oxford 100

mm^2 UltimMax SDD EDS X-ray detector. Intensity correlations between pairs of elements were obtained using an in-house MatLab script on coarsened image data (coarsening factor of 44). Image areas with very low element abundance were ignored in this analysis.

Results

Petrography and fluid inclusion paleothermometry

In samples from both localities, calcite veins containing metalliferous filaments vary up to about 2 mm in thickness, and contain two distinct generations of calcite (**Fig 2A**) as well as some minor brucite. The remainder of the host rock comprises ~90% serpentine, with the rest dominated by relict clinopyroxene, orthopyroxene, and olivine, together with hematite, chlorite, and minor secondary minerals. The calcite veins appear to correspond to the "ribbon" veins described from the same ophicalcite unit by Treves et al. (1995), who noted the presence of "scattered hematite crystals". The inner part of every filament-bearing vein is composed of colorless, cloudy, inclusion-rich, blocky or weakly fibrous calcite ("Calcite-1") with well developed calcite cleavage and an irregular, variably distinct median suture (**Fig 2A, B**). A distinct, red-brown generation of ferroan calcite ("Calcite-2") commonly occurs between the colorless inner calcite and the wall rock (on one or both sides of the vein); this mineral is strongly fibrous and varies greatly in opacity because of finely disseminated metal oxide impurities (**Fig 2A, B**). The fibres are oriented parallel to the direction of vein opening, i.e., approximately perpendicular to the vein walls. Two-phase (liquid + vapour) fluid inclusions

were identified within Calcite-1 in a sample from Locality 1, and indicated homogenization temperatures of 121–159 °C (**Supplementary Data Table 1; Supplementary Fig 1**).

Filaments: morphology and composition

At both localities, Calcite-1 contains slender, curving, opaque filaments composed of metalliferous minerals. These filaments are connected to the vein walls, to the contact between Calcite-1 and Calcite-2, to patchy opaque wall-lining cements, and to each other (**Fig 2A–C**). Filaments are concentrated in mm-scale regions, where they occur on both sides of the vein, usually oriented nearly orthogonally to the walls. One filament was observed bridging the full width of the Calcite-1 portion of a vein (**Fig 2E**). Filaments range up to a few hundred µm in length within the field of view afforded by thin sections. Of eighty-six filaments measured, the median thickness was 4.7 µm; the mean was 5.9 µm. 55% were between 2 and 5 µm; the rest were thicker (up to a maximum of 19.0 µm; the distribution is positively skewed). Thickness is typically constant along the length of each filament, but a few swell towards the tip (**Fig 2F**). Branching is common both towards and away from the vein walls and occurs at various angles, typically >45°. (**Fig 2B, C, E–K**). Rarely, filaments occur in densely packed clusters (**Fig 2I**). SRXTM revealed that filaments within these clusters are strongly interconnected by apparent branches (**Fig 2J,K; Supplementary Video**). Many filaments are patchy or diffuse (e.g, **Fig 2H**), and some are interrupted by short gaps (e.g, **Fig 2H, L**). Some neighbouring filaments glance each other tangentially but can misleadingly appear to merge because of their diffuse microcrystalline margins, particularly in SRXTM renderings that interpolate a surface around these margins. Thus, close scrutiny of the apparent "X"-junctions in these renderings shows that

the filaments do not penetrate each other centrally (e.g., **Fig 2L**). Many of the branches appear genuine, however.

Reflected-light optical microscopy, SEM/STEM imaging and EDS mapping reveal that the filaments are composed of two minerals present in two or three concentric layers, with a circular or slightly elliptical overall cross-section in the most well defined examples (**Fig 3A,B**). Most filaments possess a core and diffuse outermost layer dominated by platy hematite with a reflective metallic lustre; the identity of this mineral is confirmed by Raman spectroscopy and electron diffractometry (**Supplementary Fig 2**; crystallographic d-spacings of 0.37, 0.27, 0.25 and 0.16 nm). Most filaments also contain a Mg-silicate mineral as a discrete layer between the core and the outer layer (**Fig 3A**), although in a minority of filaments the two minerals are both present together in a single undifferentiated structure (**Fig 3B, Supplementary Fig 2**). Electron diffractometry suggests that the Mg-silicate mineral is, or is very similar to, talc (d-spacing = 0.93 nm; **Supplementary Fig 2**), a diagnosis supported by previous studies of the mineralogy of these rocks (e.g., Schwarzenbach, 2011) and by the presence of variable amounts of aluminium, which can substitute for both Mg and Si in the talc lattice (Deer, Howie and Zussman, 1992, p. 328). STEM-EDS imaging of an ultrathin FIB wafer cut perpendicular to the thin section surface reveals that the two minerals are very tightly associated within the filament cores, with lath- and needle-like Al-bearing Mg-silicate crystals filling the spaces between randomly oriented platy crystals of hematite (**Fig 3B**). Some filaments are surrounded by a finer-grained halo of hematite removed at a distance of some microns from the main filament (**Fig 3C**). The same two minerals occur as: (1) thin patches lining the inner edge of Calcite-1, to which some filaments are attached; (2) structureless, randomly distributed inclusions in Calcite-2; (3) pervasive secondary minerals associated with the serpentine outside the fractures. Raman spectroscopic analysis of

the filaments using two Raman instruments (with a 514 and 785nm laser respectively) failed to detect any carbonaceous material that might have corresponded to endogenous organic matter. No excess (i.e., non-carbonate) carbon was observed in EDS maps of the filaments, and no non-carbonate carbonaceous particles were evident in high-resolution STEM imagery.

Laminated cements and globular microstructures

Various other organized microstructures are observed in Calcite-1, which share the bimineralic composition of the filaments. These include laminated regions in the wall-lining cements to which some filaments are attached (**Fig 4A)**, and dome-like, globular and botryoidal masses up to hundreds of microns in size, many of which are attached to filaments (**Fig 4B–G**). Non-laminated, weakly laminated, and strongly laminated masses are observed. Some of these masses somewhat resemble *Frutexites*, a branching Fe-oxide growth structure thought to originate from the growth of Fe-oxidizing microorganisms (Rodríguez-Martínez et al., 2011).

Discussion

Timing of vein and filament formation

Previous work has established that the calcite veins investigated here formed in the subseafloor during the carbonation of serpentinite in the Jurassic; a similar process is responsible for the stockwork of carbonate veins underlying the Lost City Hydrothermal Field (Treves et al., 1995; Kelley et al., 2005; Alt et al., 2012; Schwarzenbach et al., 2012, 2013). The inclusion-rich, weakly fibrous nature of Calcite-1 is typical for marine carbonate cements. The inference of a subseafloor origin is also supported by petrographic comparisons between our samples and

carbonate veins previously reported from drill cores through the oceanic crust (e.g., Milliken, 2001; Eickmann et al., 2009; Ivarsson et al., 2019). The observed fluid-inclusion homogenization temperature range of 121–159 °C for Calcite-1 is consistent with the palaeotemperature range of 49–151 °C previously obtained through oxygen isotope studies of calcite veins in the same ophicalcite unit (Schwarzenbach et al., 2013).

The opaque hematite and Mg-silicate minerals that make up the patchy cements and filaments (and are associated with serpentine outside the fractures) appear to have precipitated before Calcite-1 on the edges of what must have been open, fluid-filled fractures. This interpretation is suggested by the following observations. Firstly, calcite-1 has a blocky texture and variably distinct median suture, consistent with syntaxial growth by cavity infill. Secondly, all the observed filaments either visibly attach to the vein walls or are oriented such that they probably attach to it outside the plane of the thin section, i.e., they are not simply "floating" in the middle of the veins or penetrating through them in the manner of recent microboring endoliths. One filament is observed to span the whole width of the Calcite-1 vein-fill, connecting the opaque cements on both sides (**Fig 2D**). Thirdly, some filaments (e.g., **Fig 2G**) are interrupted by short gaps without any concomitant interruption in the calcite, implying that the calcite post-dates the filaments (and calcite precipitation may have disrupted them). Fourthly, bright-field STEM images show that individual carbonate grains terminate at the edge of the filaments rather than continuing through them, again implying that the calcite post-dates the filaments (**Supplementary Fig 2D**). Fifthly, the hematite and Mg-silicate that make up the filaments are microscopically disseminated through the serpentine outside the calcite veins. Fe-oxyhydroxides (potential precursors to hematite) and talc-like Mg-silicates are known to form via the

subseafloor alteration of serpentine by seawater (Geilert et al., 2020), so we can infer that these minerals originated very early in our samples.

Calcite-2 is fibrous, with fibres perpendicular or slightly inclined to the vein axis (rather than radiating in the manner of an isopachous marine cement); it also lacks distinct median planes. It is therefore interpreted as the product of antitaxial growth, post-dating Calcite-1 and tracking along the original vein margins on one or both sides. The brown colour of Calcite-2 probably reflects the incorporation of hematite and talc inclusions derived from the existing cements. The overall sequence of events is thus inferred to have been: (1) fracturing; (2) production of filaments and associated microstructures through, or followed by, the precipitation of hematite (or its precursors) and Mg-silicate cements in the open fractures under oxidizing conditions; (3) precipitation of Calcite-1; (4) minor vein reopening and antitaxial growth of Calcite-2 veins marginal to Calcite-1.

Are the filaments fossils?

The filaments observed in our thin sections might be interpreted as permineralized fungal hyphae or bacteria that lived as part of the deep biosphere in a Jurassic subseafloor hydrothermal system. This hypothesis explains why the filaments have circular cross-sections, curved and irregular (non-crystallographic) growth trajectories, and lifelike branching patterns; these are expected features of filamentous microorganisms. The filaments are at least as lifelike in these respects as some broadly analogous assemblages that have been interpreted as fossils (e.g., Ivarsson et al. 2008 a,b; Lindgren et al., 2010; Ivarsson et al., 2015; Bengtson et al., 2017). However, their morphology is less convincingly biogenic overall than other, more sinuous and interconnected

examples (e.g., Hofmann and Farmer (2000), Hofmann et al., (2008), and Ivarsson et al. (2011; 2013).

The filaments are thicker than the Fe-mineralized sheaths of most modern Fe-oxidizers (typically 1–2 µm, to our knowledge; e.g., Vesenka et al., 2018) although these sheaths can accumulate flocculent ferric coatings at least 10 µm thick (e.g., Schmidt et al., 2014). The large size and branching behaviour of many of the filaments in our samples are perhaps more suggestive of fungal hyphae, which typically range from 2 to 27 µm in diameter and branch at high angles (Nicolson, 1959; Bengtson et al., 2017; De Ligne et al., 2019). The interpretation of the filaments as fossil fungi has numerous precedents in other mineralized filament asssemblages from subseafloor settings (e.g., Ivarsson et al., 2008; 2011; 2012; 2013).

The hematite in the filaments and vein-wall-lining cements might be thought to have originated as Fe oxyhydroxides precipitated by Fe-oxidizing bacteria. Marine biofilms can also mediate the formation of magnesium silicate minerals such as stevensite (a potential talc precursor), which replaces bacterial filaments in some thrombolites (Burne et al., 2014). However, since talc and hematite are expected to form during the aqueous alteration of serpentine (Schwarzenbach et al., 2012; Geilert et al., 2020), and since they are not restricted to the filaments or veins in our samples but occur commonly in the surrounding matrix, we infer that these minerals probably precipitated abiotically during ophicalcitization. Speculatively, this process that could have coated and replaced organic matter; differences in coating thickness might then explain the positive skew observed in the distribution of filament diameters. A similar fossilization process is invoked by Carlsson et al. (2019), who report branching curvilinear filaments compositionally

and structurally similar to ours from calcite-filled pore spaces in pillow basalts of the Troodos Ophiolite in Cyprus. These Troodos filaments are composed largely of iron oxides mantled by an Mg-rich 2:1 clay mineral (identified as montmorillonite rather than talc). Carlsson et al. interpret these filaments as fossilized fungal hyphae, and argue that their bimineralic composition reflects sequential precipitation of hematite and clay as a replacement and coating of organic matter. Indeed, similar filaments are found in many other carbonate veins and amygdales in mafic and ultramafic oceanic crust, both in ophiolites and in subseafloor drill-cores, and have often been interpreted as biological in origin (e.g., examples tabulated in McMahon and Ivarsson, 2019). Milliken (2001) examined Cretaceous calcite veins from the Iberia Margin ophicalcite, a close geochemical analogue to the ophicalcites of Liguria, and discovered Mg-silicate and Fe-oxide cements with radiating Mg-silicate filaments. Compared to the Ligurian examples, these Iberian filaments are straighter and more densely crowded; they also lack branching, and are reportedly composed solely of Mg-silicate. Milliken interpreted these agnostically as "possibly" microbial in origin. Carbonate-filled vugs and veins from Cretaceous and Palaeogene basaltic seamounts in the Pacific Ocean have yielded numerous assemblages of curvilinear, branched filaments composed of clays and Fe-oxides, typically 2–5 µm in diameter (e.g., Ivarsson et al., 2008; 2011; 2012; 2013). It is important to note that filaments in some Eocene calcite veins in these seamounts consist largely of remnant organic matter, including chitin, which can be detected with fluorescent stains (Ivarsson et al., 2012). This observation implies that these organically preserved specimens are fossilized chasmoendolithic fungal hyphae. The fact that they are variously associated with, coated, and replaced by Fe oxides and clay minerals also implies a biological origin for morphologically and contextually similar filaments that are preserved inorganically and lack organic carbon (Ivarsson et al., 2008). Purported filamentous microfossils

consisting of an iron-rich core mantled by a silicate/aluminosilicate phase have also been reported from the non-marine deep biosphere (e.g., Lindgren et al., 2010; Drake et al., 2017). Drake et al. (2017) describe probable fungal hyphae from a deep granitic borehole that offer a snapshot of the fossilization process in action; some filaments are still organic in composition, while others are replaced to varying degrees by Fe oxide (forming a "central strand") and Fe-, Mg-, and Ca-rich clay minerals (forming a "margin").

In carbonate veins from subseafloor drill-cores, *Frutexites* structures are commonly found in close proximity to filaments (e.g., Eickmann et al., 2008; Ivarsson et al., 2019). Although more finely laminated and fractal-like, some of these *Frutexites* are broadly similar to the globular structures described in the present study (**Fig 4**), even showing alternating bands of Fe-oxides and Mg-silicates with minor Al (Ivarsson et al., 2019). *Frutexites* is generally interpreted as a kind of "microstromatolite" formed by the growth of Fe-oxidizing bacterial biofilms, although the precise role of abiotic versus biotic processes in forming these structures is unclear (e.g., Rodríguez-Martínez et al., 2011; Ivarsson et al., 2020). The simple morphology of the globular, laminated structures in our samples is less suggestive of microbial growth than those described by, e.g., Eickmann et al., (2008), Bengtson et al. (2014), and Ivarsson et al. (2019), and more reminiscent of abiotic processes.

Are the filaments pseudofossils?

The hematite+Mg-silicate filaments might also be interpreted as fossilized metal-silica membrane structures related to "chemical gardens": abiotic self-organized structures that grow through chemiosmotic reaction-diffusion-precipitation processes under far-from-equilibrium

conditions. In a well-known laboratory demonstration, chemical gardens are produced by dissolving "seed" grains of transition-metal salts into alkaline solutions rich in carbonate or silicate. The resulting acid–base reaction produces a semipermeable envelope of colloidal, hydrous carbonate or silica around the dissolving seed. Inflow of water increases the osmotic pressure until the envelope ruptures, expelling a thin, acidic jet around which new membrane material immediately forms. The resulting finger-like tubes rapidly acquire an inner coating of metal (oxyhydr)oxide, which gradually thickens and can ultimately occupy most of the interior space, forming bimineralic tubes and filaments of concentrically organised amorphous silica and metal oxyhydroxides (Barge et al., 2015, McMahon, 2019; Kotopoulou et al., in press). Similar "chemobrionic" processes are involved in diverse phenomena, from the production of carbonate and sulfide chimneys at alkaline (serpentinization-driven) and acidic hydrothermal vents (respectively) to the development of tubules and "whiskers" during the corrosion of iron and steel (Barge et al., 2015). In nature, such processes may occur wherever reactive metalliferous mineral particles or solutions come into contact with carbonate- and/or silica-rich alkaline fluids (Barge et al., 2015; McMahon, 2019). Recent work confirms that highly alkaline, silica-rich fluids produced during the natural alteration of serpentinite generate filamentous chemical gardens when introduced experimentally to appropriate metal salts (Garcia-Ruiz et al., 2017). Thus, chemobrionic chemistry provides an especially appropriate abiotic explanation for the presence of metalliferous oxide+silicate filaments in our samples, which formed during the alteration of serpentinite. One might speculate that the "seed" material from which filaments grew could have been ferrous sulfide phases that were oxidized to Fe^{3+} and SO_4^{2-} during the ophicalcitization process — Fe-bearing sulfides are still present in some calcite veins in the Ligurian serpentinites, and are pseudomorphed by hematite in some of the ophicalcites

(Schwarzenbach et al., 2012) — but it may be that chemobrionic structures formed more directly through serpentine decomposition under far-from-equilibrium conditions.

Chemical garden filaments have important features in common with our samples, including circular cross-sections, concentric chemical zonation, constant-thickness growth, curved trajectories, infrequent swellings, and lifelike branching (McMahon, 2019; see Figure 1 a–h in that paper). The Ligurian filaments are very similar in size to chemical gardens described by McMahon (2019), which were grown at room temperature and pressure from finely sieved (<63 µm) grains of hydrated ferrous sulphate placed into a sodium silicate solution (**Fig 5**). Both the Ligurian filaments and these laboratory-grown chemical gardens show positively skewed diameter distributions, with few filaments less than 2 µm or greater than 10 µm in diameter, and modal ranges of 3–4 µm.

The Ligurian filaments are structurally similar to abiotic chemical gardens produced from Fe-salts dissolved in silica, in as much as they might be said to consist of silicon-rich "tubes" with iron oxide on the interior (**Fig 3a**; cf. McMahon, 2019; Kotopoulou et al., in press). However, the Ligurian filaments also contain Mg and Al as major and minor constituents (respectively) of the silicate layer, but not of the Fe-oxide layer. To our knowledge, chemical gardens have not previously been described in the literature from polymetallic Fe-Mg-Al seed material. We therefore conducted a simple experiment to determine whether Mg and Al would partition into the Si-rich layers or the Fe-oxhydroxide-rich layers of a chemical garden. We produced tubular chemical gardens by dissolving an Fe,Mg,Al-sulfate salt (a member of the copiapite family) in sodium silicate solution, and examined them in cross-section (**Figure 6**). EDX counts and maps

of the tube walls showed clear chemical zonation into discrete layers dominated by Fe and Si, respectively. Mg and Al partitioned preferentially into Si-rich layers within the tube walls, while Fe precipitated internally and on outer surfaces (**Figure 6A**). For one tube, we computed spatial correlations between different elements using the coarsened EDX maps (**Figure 6B**). Overall, stronger spatial associations were observed between Mg and Si (correlation coefficient=0.71), Al and Si (0.72), and Mg and Al (0.55) than between Fe and Mg (0.48), Fe and Si (0.19), or Fe and Al (-0.20). These results suggest that the partitioning of Fe and Mg between oxides and silicates in the Ligurian filaments — as well as their overall spatial arrangements — are broadly in agreement with the chemical garden hypothesis. This agreement would be more compelling if crystalline Mg silicates and Fe oxides could be shown to result from the diagenetic and metamorphic maturation and recrystallization of the amorphous/poorly crystalline, hydrous materials precipitated in chemical gardens.

We also cannot exclude the possibility that the Ligurian filaments are alteration products of asbestiform serpentine or clay minerals. It has been observed that fibrous crystals are long and flexible, and can somewhat resemble endolithic microbial filaments (Muscente et al., 2018); they can also radiate from vesicle walls in altered marine basalt (Kurnosov et al., 1995). The filaments in our samples do not consist of single or bundled crystal fibres, as seen in asbestiform minerals, but might perhaps derive from the breakdown and recrystallization of fibres. Speculatively, such an alteration process might soften the edges of serpentine fibres to produce rounded and diffuse cross-sections like those observed in our filaments. Contiguity with the wall-lining cements could be explained by the concomitant alteration of the non-fibrous serpentine in the fracture walls. However, the constant-thickness branching and rare "swellings" observed in many

filaments are difficult to explain by this mechanism, rendering an asbestiform mineral origin less likely.

The *Frutexites*-like globular and botryoidal laminated structures in our samples are morphologically simple and might also be explained by abiotic self-organization processes. Indeed, stromatolite-like forms characterized by convex laminations are mimicked by a variety of abiotic growth processes including diffusion-limited aggregation and oscillating chemical reactions (McLoughlin et al., 2008; Chan et al., 2019; Papineau, 2020; Johannessen et al., 2020). Fe-oxide "plumes" in agates can show very similar features to *Frutexites* (including microscopic laminations) and have generally not been interpreted as microbial in origin, although these materials are very poorly understood.

Biogenicity criteria

Several lists of biogenicity criteria have been developed to assess the origins of candidate biosignatures. Many workers have emphasized that the (palaeo)environment must be habitable for the claim of biogenicity to be tenable (e.g., Brasier and Wacey, 2012). We do not know for sure whether the calcite-filled fractures investigated here were once habitable, although the example of the Lost City Hydrothermal Field, where calcifying subsurface fluids support a small amount of microbial biomass under rather extreme conditions, provides an interesting modern analogue (Kelley et al., 2005; Lang and Brazelton, 2020). Our fluid-inclusion microthermometry results show that the calcite-forming fluid circulated at temperatures of 121–159 °C, i.e., generally higher than the upper limit for the reproduction of known hyperthermophiles (122 °C; Takai et al., 2008). Similarly, filaments described from Pacific subseafloor calcite veins by

Ivarsson et al. were entombed in calcite veins with homogenization temperatures of ~130 °C (Ivarsson et al., 2009). However, in both cases, microbial communities could have lived in cooler conditions before an increase in temperature drove the precipitation of calcite.

The apparent absence of carbonaceous residues in the filaments is a clear failure to meet a widely accepted biogenicity criterion, and makes their biogenicity more doubtful than several other examples of similar filament assemblages that do contain organic matter (e.g., Ivarsson et al., 2012, 2018). Nevertheless, this absence does not refute the hypothesis that the structures in our samples are biogenic, for (at least) the following three reasons. Firstly, the mineral filaments and sheaths excreted by modern Fe-oxidizing bacteria commonly contain only a little organic matter and are vacated by cells during life (Emerson and Moyer, 2002; Chan et al., 2011; Picard et al., 2015). Secondly, the abundance of hematite in our samples indicates oxidizing conditions that would not have been conducive to the preservation of reduced carbonaceous matter; the total organic carbon content in the Ligurian ophicalcites is typically only a few hundred ppm (Schwarzenbach et al., 2013). The lack of organic carbon in some purported bioalteration textures in subseafloor volcanic glass (it is present in others) has likewise been explained as a consequence of decomposition (Thorseth et al., 2003). Thirdly, it is possible that small amounts of carbon were actually present in our samples but escaped detection, perhaps partly because mineral phases such as hematite dwarfed and obscured the diagnostic carbon bands in Raman spectra (e.g., Brolly et al., 2016), and only a few filaments could be examined by STEM. In any case, even if organic matter had been detectable in our filaments, it would not have shown conclusively that they are biogenic (although analysis of its composition might do so). Fischer-Tropsch-type synthesis occurs in serpentinizing systems and can generate organic solids (Milesi

et al., 2016). Abiotic chemical garden filaments tend to adsorb organic matter and promote its condensation (Kotopoulou et al., 2020). Even if there were demonstrably biogenic organic matter in our samples, it might have been incorporated into abiotic filaments, such that the structures themselves would still not be morphological fossils.

It has been argued that fossil chasmoendolithic filaments can be recognised by a distinctive suite of features, namely: (i) evidence of growth into a fluid-filled fracture; (ii) circular cross-sections of "non-uniform" diameter; (iii) curvilinear, branched morphologies with terminal swellings or internal septae; (iv) Fe-oxide or clay composition (McLoughlin et al., 2010). The Ligurian filaments meet these criteria. However, McMahon (2019) has shown that these same features are consistent with abiotic filament growth by chemobrionic processes. Johannessen et al. (2020) recently proposed more detailed criteria for discriminating between abiotic and biotic modes of origin for silicified Fe-oxide filaments and tubules in hydrothermal cherts, which commonly lack carbonaceous residues. The abiotic processes they have in mind are, specifically, diffusion-limited aggregation and chemobrionic self-organization (chemical gardens). Although our materials are not cherts, some of the proposed criteria are relevant to the present samples, since they concern the size, branching habit and orientation of the filaments, and not the nature of the mineral matrix. For example, Johannessen et al. suggest that filaments and tubes of diameter ~1 µm may be more likely to be bacteriogenic than those of diameter ~10 µm. Most of the filaments observed in the present study fall in between this range (**Fig 5a**) but none are as narrow as 1 um and many are thicker than 10 µm, even if one considers only their hematite-rich cores. In any case, our filaments might have been thickened by coatings, and might be fungal rather than

bacterial; fungal hyphae can be tens of microns in diameter. Overall, the thickness of the filaments in our samples does not resolve their biogenicity.

Johannessen et al. (2020) also highlight branching style as a potential means to discriminate between biotic and abiotic filaments. They propose that sequential bifurcation is typical of microbial filaments as a consequence of binary cell division during growth, whereas nodes with multiple branches are characteristic of diffusion-limited abiotic growth structures. However, sequentially bifurcating Fe-(oxyhydr)oxide filaments have been produced in abiotic chemical garden experiments (McMahon, 2019). Thus, although a few of the filaments in our samples show sequential bifurcation, this branching style does not resolve their biogenicity.

Finally, Johannessen et al. also suggest that populations of abiotic filaments tend to grow parallel to each other but with shifts in direction at a larger scale, whereas bacterial filaments show semi-parallel growth due to chemotaxis (assuming a stable redox gradient). The filaments in our samples are generally oriented normal to the surfaces on which they grew; a slight preference for this direction is retained even in the most densely clustered assemblages (**Fig 2H**). This habit of surface-normal orientation has previously been noted in fracture-dwelling filamentous microorganisms but is not a reliable biosignature since abiotic mineral growth processes commonly also proceed normal to the nucleation surface (and might well follow chemical gradients). Thus, the spatial orientation of our filaments does not resolve their biogenicity.

Dubiofossils

Having considered the morphology, spatial organization, chemical composition and mineralogy of the filaments in our samples, as well as the geochemical context in which they formed, we remain unable to reject either the hypothesis that they are fossils or the hypothesis that they are abiotic pseudofossils. Both scenarios are plausible, and in our view equally interesting. Established "biogenicity criteria" do not settle the question, although they do suggest ways in which the Ligurian filaments represent less compelling evidence for life than they might have done, e.g., had they contained organic carbon.

Historically, there have been two schools of thought on how to evaluate and present such ambiguous materials in the literature. One popular view is that they simply "should not be accepted as being of biological origin until possibilities of their non-biological origin have been tested and can be falsified" (Brasier et al., 2004). This approach treats these non-biological "possibilities" as "null hypotheses", and places the burden of evidence on those proposing biogenicity (Brasier and Wacey, 2012). However, this strategy can actually exacerbate the very risk of "false positives" that it was designed to avert. We suspect that the available "abiotic null hypotheses" very often do not fit the facts — and so are "rejected" in favour of biogenicity — because they are the *wrong* null hypotheses. In other words, many fossil-like microstructures are likely to be the products of abiotic processes that have not yet been discovered or brought to the attention of palaeontologists; the *right* "null hypotheses" are thus not yet available. Perhaps the most unusual aspect of the present case study is precisely the fact that the far-from-equilibrium, highly alkaline geochemical context furnishes a fairly obvious "null hypothesis", i.e., that the structures we describe are ancient chemical gardens. Arguably, however, the same

mechanism has been missed in other cases, leading to dubious claims to have successfully "rejected" an abiotic origin for purported fossils (e.g., Dodd et al., 2017).

The alternative strategy recommended by, for example, Hofmann (1972) and Buick (1990), is to describe inconclusively fossil-like features as "dubiofossils" (Hofmann, 1972). The use of this neutral term avoids shoehorning ambiguous objects into favoured categories on the basis of inconclusive (or cherry-picked) evidence or the falsification of inappropriate "null hypotheses". Brasier et al. (2004) expressed concern that "the dubiofossil concept may encourage fuzzy thinking in an area (the prebiotic-biotic boundary) where this now urgently needs to be avoided." Admittedly, anything resembling a fossil is ultimately a fossil or a pseudofossil, and we should not elide this distinction. But the term "dubiofossil" remains a helpful stopgap, like the palaeontological term "problematicum". If desired, the dubiofossil category can be made more precise by scoring the quality of the evidence using biogenicity criteria, even if they do not finally compel either a biotic or an abiotic interpretation (Buick, 1990; Neveu et al., 2018; McLoughlin and Grosch, 2015). Thus, in Buick's (1990) scheme, candidate microbial fossils in Archean rocks should meet a hierarchical series of seven criteria, in order of importance: (1) occurrence within a petrographic thin section; (2) occurrence within a sedimentary or low-grade metasedimentary rock; (3) a size consistent with a microbial origin; (4) a kerogenous composition; (5) occurrence in a population with a shared morphology; (6) hollowness; and (7) morphological complexity or elaboration. On this scheme, objects meeting all seven criteria are to be accepted as microfossils, while those complying only with the first four are to be considered dubiofossils. Similar schemes can be devised for other contexts more relevant to the present study. For example, McLoughlin and Grosch (2015) present a hierarchical scheme for

evaluating the biogenicity of metavolcanic- and ultramafic-hosted microalteration textures. These criteria concern, in the following order, "textural context and syngenicity", "morphology", "geological setting", "geochemistry", and "putative growth pattens"; with further subdivisions addressing different aspects of each of these themes. On our reading (adjusting for the fact that McLoughlin and Grosch focus on bioalteration textures and encrusted spheroids rather than filamentous body fossils), the Ligurian filaments reported here would qualify as "tentative biosignatures" on this scheme, since they are morphologically complex but lack geochemical evidence for life. We prefer "dubiofossils" to "tentative biosignatures" since "dubio-" (i.e., doubtful) seems a more apt qualifier than "tentative" (i.e., provisional) in this case, but the underlying concept is clearly similar.

Regardless of the preferred nomenclature, if dubiofossils are found on Mars, they should be presented neutrally and neither overinterpreted as fossils nor prematurely dismissed as pseudofossils until scientific advances resolve their biogenicity satisfactorily. If known processes of pseudofossil formation are relevant to the object of study then by all means they should be investigated and falsified if possible, but this is not necessarily enough to show that the object is or is not a fossil. Ambiguous results are to be expected in life-detection research and must be handled with appropriate objectivity (Cleland, 2019).

Conclusion: dubiofossils on Mars?

The occurrence of dubiofossils — and lack of definitive fossils — in the serpentinization-associated calcite veins of the Ligurian ophiolite highlights the risk that similarly ambiguous

microstructures may be found in samples returned from geologically similar targets on Mars. Serpentinisation-associated carbonates occur in the Northeast Syrtis region of Mars, which was a shortlisted landing site for the Mars 2020 rover (Perseverance) partly in the hope of obtaining samples from rock-hosted subsurface palaeohabitats (e.g., Onstott et al. 2019). Although this site was rejected in favour of Jezero Crater, recent work has highlighted the presence of olivine-carbonate units in Jezero Crater, which may result from serpentinization driven by magmatic or impact-related heating (Brown et al., 2020). Recovery of samples from this material, if it can be accessed, may well be worthwhile as part of a comprehensive biosignature search strategy, but may lead to agnostic conclusions like those of the present study. To avoid such an impasse, more work is still needed to advance our understanding of abiotic mineral morphogenesis, microbial taphonomy and micro-analytical palaeobiology. The resulting data will inform the development of new, more definitive and robust protocols for biogenicity determination, e.g., multiparametric statistical comparisons that show quantitatively whether particular dubiofossil assemblages more closely resemble true fossils or pseudofossils (Rouillard et al., 2021). In the meantime, we recommend that fossil-like structures whose biogenicity cannot be determined should be reported as such, and not overinterpreted either as biological or non-biological objects.

Author Disclosure Statement

No competing financial interests exist.

Acknowledgments

References

Alt, J. C., Shanks III, W. C., Crispini, L., Gaggero, L., Schwarzenbach, E. M., Früh-Green, G. L., & Bernasconi, S. M. (2012). Uptake of carbon and sulfur during seafloor serpentinization and the effects of subduction metamorphism in Ligurian peridotites. *Chemical Geology*, *322*, 268-277.

Barge, L. M., Cardoso, S. S., Cartwright, J. H., Cooper, G. J., Cronin, L., De Wit, A., ... & Jones, D. E. (2015). From chemical gardens to chemobrionics. *Chemical Reviews*, *115*(16), 8652-8703.

Bengtson, S., Rasmussen, B., Ivarsson, M., Muhling, J., Broman, C., Marone, F., ... & Bekker, A. (2017). Fungus-like mycelial fossils in 2.4-billion-year-old vesicular basalt. *Nature Ecology & Evolution*, *1*(6), 1-6.

Bigazzi, G., Ferrara, G., & Innocenti, F. (1972). Fission track ages of gabbros from Northern Apennines ophiolites. *Earth and Planetary Science Letters*, *14*(2), 242-244.

Blamey, N. J., Parnell, J., McMahon, S., Mark, D. F., Tomkinson, T., Lee, M., ... & Flemming, R. L. (2015). Evidence for methane in Martian meteorites. *Nature Communications*, *6*(1), 1-7.

Bortolotti, V., Principi, G., and Treves, B. (2001). Ophiolites, Ligurides, and the Tectonic Evolution from Spreading to Convergence of a Mesozoic Western Tethys Segment. In Vai, G.B. and Martini, I.P., eds., *Anatomy of an Orogen: The Apennines and Adjacent Mediterranean Basins* (pp. 151–164). Springer Netherlands.

Brasier, M., Green, O., Lindsay, J., & Steele, A. (2004). Earth's Oldest (∼ 3.5 Ga) Fossils and the Early Eden Hypothesis': Questioning the Evidence. *Origins of Life and Evolution of the Biosphere*, *34*(1-2), 257-269.

Brasier, M. D., & Wacey, D. (2012). Fossils and astrobiology: new protocols for cell evolution in deep time. *International Journal of Astrobiology*, *11*(4), 217-228.

Brolly, C., Parnell, J., & Bowden, S. (2016). Raman spectroscopy: Caution when interpreting organic carbon from oxidising environments. *Planetary and Space Science*, *121*, 53-59.

Brown, A. J., Viviano, C. E., & Goudge, T. A. (2020). Olivine-Carbonate Mineralogy of the Jezero Crater Region. *Journal of Geophysical Research: Planets*, *125*(3), e2019JE006011.

Buick, R. (1990). Microfossil recognition in Archean rocks; an appraisal of spheroids and filaments from a 3500 my old chert-barite unit at North Pole, Western Australia. *Palaios*, *5*(5), 441-459.

Burne, R. V., Moore, L. S., Christy, A. G., Troitzsch, U., King, P. L., Carnerup, A. M., & Hamilton, P. J. (2014). Stevensite in the modern thrombolites of Lake Clifton, Western Australia: A missing link in microbialite mineralization?. *Geology*, *42*(7), 575-578.

Carlsson, D.-T., Ivarsson, M., & Neubeck, A. (2019). Fossilized endolithic microorganisms in pillow lavas from the Troodos Ophiolite, Cyprus. *Geosciences, 9,* 456.

Chan, M. A., Hinman, N. W., Potter-McIntyre, S. L., Schubert, K. E., Gillams, R. J., Awramik, S. M., ... & Jia, T. Z. (2019). Deciphering biosignatures in planetary contexts. *Astrobiology*, *19*(9), 1075-1102.

Changela, H. G., & Bridges, J. C. (2010). Alteration assemblages in the nakhlites: Variation with depth on Mars. *Meteoritics & Planetary Science*, *45*(12), 1847-1867.

Cleland, C. E. (2019). *The Quest for a Universal Theory of Life: Searching for Life as we don't know it* (pp. 172–176). Cambridge University Press.

De Ligne, L., de Ulzurrun, G. V. D., Baetens, J. M., Van den Bulcke, J., Van Acker, J., & De Baets, B. (2019). Analysis of spatio-temporal fungal growth dynamics under different environmental conditions. *IMA fungus*, *10*(1), 1-13.

Dodd, M. S., Papineau, D., Grenne, T., Slack, J. F., Rittner, M., Pirajno, F., ... & Little, C. T. (2017). Evidence for early life in Earth's oldest hydrothermal vent precipitates. *Nature*, *543*(7643), 60-64.

Ehlmann, B. L., Mustard, J. F., & Murchie, S. L. (2010). Geologic setting of serpentine deposits on Mars. *Geophysical Research Letters*, *37*(6).

Eickmann, B., Bach, W., Rosner, M., & Peckmann, J. (2009). Geochemical constraints on the modes of carbonate precipitation in peridotites from the Logatchev Hydrothermal Vent Field and Gakkel Ridge. *Chemical Geology*, *268*(1-2), 97-106.

Emerson, D., & Moyer, C. L. (2002). Neutrophilic Fe-oxidizing bacteria are abundant at the Loihi Seamount hydrothermal vents and play a major role in Fe oxide deposition. *Applied and Environmental Microbiology*, *68*(6), 3085-3093.

Fonti, S., & Marzo, G. A. (2010). Mapping the methane on Mars. *Astronomy & Astrophysics*, *512*, A51.

García Ruiz, J. M., Carnerup, A., Christy, A. G., Welham, N. J., & Hyde, S. T. (2002). Morphology: an ambiguous indicator of biogenicity. *Astrobiology*, *2*(3), 353-369.

García-Ruiz, J. M., Nakouzi, E., Kotopoulou, E., Tamborrino, L., & Steinbock, O. (2017). Biomimetic mineral self-organization from silica-rich spring waters. *Science Advances*, 3(3), e1602285.

Geilert, S., Grasse, P., Wallmann, K., Liebetrau, V., & Menzies, C. D. (2020). Serpentine alteration as source of high dissolved silicon and elevated δ 30 Si values to the marine Si cycle. *Nature Communications*, *11*(1), 1-11.

Giuranna, M., Viscardy, S., Daerden, F., Neary, L., Etiope, G., Oehler, D., ... & Cardesín-Moinelo, A. (2019). Independent confirmation of a methane spike on Mars and a source region east of Gale Crater. *Nature Geoscience*, *12*(5), 326-332.

Hofmann, H. J. (1972, August). Precambrian remains in Canada: fossils, dubiofossils, and pseudofossils. In *Proceedings of the 24th International Geological Congress, Section* (Vol. 1, pp. 20-30).

Hofmann B. A., & Farmer, J. D. (2000). Filamentous fabrics in low–temperature mineral assemblages: are they fossil biomarkers? Implications for the search for a subsurface fossil record on the early Earth and Mars. *Planet Space Sci*, *48*, 1077-1086.

Hofmann, B. A., Farmer, J. D., Von Blanckenburg, F., & Fallick, A. E. (2008). Subsurface filamentous fabrics: an evaluation of origins based on morphological and geochemical criteria, with implications for exopaleontology. *Astrobiology*, *8*(1), 87-117.

Howie, R. A., Zussman, J., & Deer, W. (1992). *An introduction to the rock-forming minerals* (p. 696). Longman.

Ivarsson, M., Bengtson, S., Belivanova, V., Stampanoni, M., Marone, F., & Tehler, A. (2012). Fossilized fungi in subseafloor Eocene basalts. *Geology*, *40*, 163-166.

Ivarsson, M., Bengtson, S., Skogby, H., Belivanova, V., & Marone, F. (2013). Fungal colonies in open fractures of subseafloor basalt. *Geo-Marine Letters*, *33*(4), 233-243.

Ivarsson, M., Broman, C., Gustafsson, H., & Holm, N. G. (2015). Biogenic Mn-oxides in subseafloor basalts. *PLoS One*, *10*(6), e0128863.

Ivarsson, M., Broman, C., & Holm, N. G. (2011). Chromite oxidation by manganese oxides in subseafloor basalts and the presence of putative fossilized microorganisms. *Geochemical Transactions*, *12*(1), 1-10.

Ivarsson, M., Drake, H., Neubeck, A., Sallstedt, T., Bengtson, S., Roberts, N., & Rasmussen, B. (2020). The fossil record of igneous rock. *Earth-Science Reviews*, 103342.

Ivarsson, M., Bach, W., Broman, C., Neubeck, A., & Bengtson, S. (2018). Fossilized life in subseafloor ultramafic rocks. *Geomicrobiology Journal*, *35*(6), 460-467.

Ivarsson, M., Lausmaa, J., Lindblom, S., Broman, C., Holm, N. G. (2008a). Fossilized microorganisms from the Emperor Seamounts: implications for the search for a subsurface fossil record on Earth and Mars. *Astrobiol* 8: 1139-57.

Ivarsson, M., Sallstedt, T., & Carlsson, D. T. (2019). Morphological biosignatures in volcanic rocks–applications for life detection on Mars. *Frontiers in Earth Science*, *7*, 91.

Johannessen, K. C., McLoughlin, N., Vullum, P. E., & Thorseth, I. H. (2020). On the biogenicity of Fe-oxyhydroxide filaments in silicified low-temperature hydrothermal deposits: Implications for the identification of Fe-oxidizing bacteria in the rock record. *Geobiology*, *18*(1), 31-53.

Kelley, D. S., Karson, J. A., Früh-Green, G. L., Yoerger, D. R., Shank, T. M., Butterfield, D. A., ... & Jakuba, M. (2005). A serpentinite-hosted ecosystem: the Lost City hydrothermal field. *Science*, *307*(5714), 1428-1434.???

Klein, F., Humphris, S. E., Guo, W., Schubotz, F., Schwarzenbach, E. M., & Orsi, W. D. (2015). Fluid mixing and the deep biosphere of a fossil Lost City-type hydrothermal system at the Iberia Margin. *Proceedings of the National Academy of Sciences*, *112*(39), 12036-12041.

Klein, F., & McCollom, T. M. (2013). From serpentinization to carbonation: new insights from a CO_2 injection experiment. *Earth and Planetary Science Letters*, *379*, 137-145.

Kotopoulou, E., Lopez-Haro, M., Calvino Gamez, J. J., & Garcia-Ruiz, J. M. Nanoscale anatomy of iron-silica self-organized membranes: implications for prebiotic chemistry. *Angewandte Chemie*.

Krasnopolsky, V. A., Bjoraker, G. L., Mumma, M. J., & Jennings, D. E. (1997). High-resolution spectroscopy of Mars at 3.7 and 8 μm: A sensitive search for H2O2, H2CO, HCl, and CH4, and detection of HDO. *Journal of Geophysical Research: Planets*, *102*(E3), 6525-6534.

Kurnosov, V., Zolotarev, B., Eroshchev-Shak, V., Artamonov, A., Kashinzev, G., & Murdmaa,I. (1995). Alteration of basalts from the West Pacific Guyots, Legs 134 and 144. *Proceedings of the Ocean Drilling Program, Scientific Results,* 144(28), 475–491.

Lang, S. Q., & Brazelton, W. J. (2020). Habitability of the marine serpentinite subsurface: a case study of the Lost City hydrothermal field. *Philosophical Transactions of the Royal Society A*, *378*(2165), 20180429.

Lindgren, P., Ivarsson, M., Neubeck, A., Broman, C., Henkel, H., & Holm, N. G. (2010). Putative fossil life in a hydrothermal system of the Dellen impact structure, Sweden. *International Journal of Astrobiology*, 9(3), 137.

Marone, F., & Stampanoni, M. (2012). Regridding reconstruction algorithm for real-time tomographic imaging. *Journal of synchrotron radiation*, *19*(6), 1029-1037.

McKinley, J. P., Stevens, T. O., & Westall, F. (2000). Microfossils and paleoenvironments in deep subsurface basalt samples. *Geomicrobiology Journal*, *17*(1), 43-54.

McLoughlin, N., & Grosch, E. G. (2015). A hierarchical system for evaluating the biogenicity of metavolcanic-and ultramafic-hosted microalteration textures in the search for extraterrestrial life. *Astrobiology*, *15*(10), 901-921.

McLoughlin, N., Staudigel, H., Furnes, H., Eickmann, B., & Ivarsson, M. (2010). Mechanisms of microtunneling in rock substrates: distinguishing endolithic biosignatures from abiotic microtunnels. *Geobiology*, *8*(4), 245-255.

McLoughlin, N., Wilson, L. A., & Brasier, M. D. (2008). Growth of synthetic stromatolites and wrinkle structures in the absence of microbes–implications for the early fossil record. *Geobiology*, *6*(2), 95-105.

McMahon, S. (2019). Earth's earliest and deepest purported fossils may be iron-mineralized chemical gardens. *Proceedings of the Royal Society B*, *286*(1916), 20192410.

McMahon, S., & Ivarsson, M. (2019). A new frontier for palaeobiology: Earth's vast deep biosphere. *Bioessays*, *41*(8), 1900052.

Milesi, V., McCollom, T. M., & Guyot, F. (2016). Thermodynamic constraints on the formation of condensed carbon from serpentinization fluids. *Geochimica et Cosmochimica Acta*, *189*, 391-403.

Mumma, M. J., Villanueva, G. L., Novak, R. E., Hewagama, T., Bonev, B. P., DiSanti, M. A., ... & Smith, M. D. (2009). Strong release of methane on Mars in northern summer 2003. *Science*, *323*(5917), 1041-1045.

Muscente, A. D., Czaja, A. D., Tuggle, J., Winkler, C., & Xiao, S. (2018). Manganese oxides resembling microbial fabrics and their implications for recognizing inorganically preserved microfossils. *Astrobiology*, *18*(3), 249-258.

Neveu, M., Hays, L. E., Voytek, M. A., New, M. H., & Schulte, M. D. (2018). The ladder of life detection. *Astrobiology*, *18*(11), 1375-1402.

Nicolson, T. H. (1959). Mycorrhiza in the Gramineae: I. Vesicular-arbuscular endophytes, with special reference to the external phase. *Transactions of the British Mycological Society*, *42*(4), 421-IN3.

Onstott, T. C., Ehlmann, B. L., Sapers, H., Coleman, M., Ivarsson, M., Marlow, J. J., ... & Niles, P. (2019). Paleo-rock-hosted life on Earth and the search on Mars: a review and strategy for exploration. *Astrobiology*, *19*(10), 1230-1262.

Papineau, D. (2020). Chemically oscillating reactions in the formation of botryoidal malachite. *American Mineralogist: Journal of Earth and Planetary Materials*, *105*(4), 447-454.

Rodríguez-Martínez, M., Heim, C. M., Quéric, N. V., & Reitner, J. (2011). Frutexites. In *Encyclopedia of Earth Sciences Series* (pp. 396-401). Springer Netherlands.

Rouillard, J., van Zuilen, M., Pisapia, C., & Garcia-Ruiz, J. M. (2021). An Alternative Approach for Assessing Biogenicity. Astrobiology, 21(2), 151-164.

Schmidt, B., Sánchez, L. A., Fretschner, T., Kreps, G., Ferrero, M. A., Siñeriz, F., & Szewzyk, U. (2014). Isolation of Sphaerotilus–Leptothrix strains from iron bacteria communities in Tierra del Fuego wetlands. *FEMS Microbiology Ecology*, *90*(2), 454-466.

Schwarzenbach, E. (2011). *Serpentinization, fluids and life: Comparing carbon and sulfur cycles in modern and ancient environments* (Doctoral dissertation, ETH Zurich).

Schwarzenbach, E. M., Früh-Green, G. L., Bernasconi, S. M., Alt, J. C., Shanks III, W. C., Gaggero, L., & Crispini, L. (2012). Sulfur geochemistry of peridotite-hosted hydrothermal

systems: comparing the Ligurian ophiolites with oceanic serpentinites. *Geochimica et Cosmochimica Acta*, *91*, 283-305.

Schwarzenbach, E. M., Lang, S. Q., Früh-Green, G. L., Lilley, M. D., Bernasconi, S. M., & Méhay, S. (2013). Sources and cycling of carbon in continental, serpentinite-hosted alkaline springs in the Voltri Massif, Italy. *Lithos*, *177*, 226-244.

Stevens, T. O., & McKinley, J. P. (1995). Lithoautotrophic microbial ecosystems in deep basalt aquifers. *Science*, *270*(5235), 450-455.

Strating, E. H., & Van Wamel, W. A. (1989). The structure of the Bracco Ophiolite complex (Ligurian Apennines, Italy): a change from Alpine to Apennine polarity. *Journal of the Geological Society*, *146*(6), 933-944.

Thorseth, I. H., Pedersen, R. B., & Christie, D. M. (2003). Microbial alteration of 0–30-Ma seafloor and sub-seafloor basaltic glasses from the Australian Antarctic Discordance. *Earth and Planetary Science Letters*, *215*(1-2), 237-247.

Treves, B. E., & Harper, G. D. (1994). Exposure of serpentinites on the ocean floor: sequence of faulting and hydrofracturing in the Northern Apennine ophicalcites. *Ofioliti*, *19*(4), 435-466.

Treves, B., Hickmott, D., & Vaggelli, G. (1995). Texture and microchemical data of oceanic hydrothermal calcite veins, Northern Apennine ophicalcites. *Ofioliti*, *20*(2), 111-122.

Vesenka, J., Havu, J., Hruby, K., & Emerson, D. (2018). A model for sheath formation coupled to motility in Leptothrix ochracea. *Geomicrobiology Journal*, *35*(5), 366-374.

Wacey, D., Battison, L., Garwood, R. J., Hickman-Lewis, K., & Brasier, M. D. (2017). Advanced analytical techniques for studying the morphology and chemistry of Proterozoic microfossils. *Geological Society, London, Special Publications*, *448*(1), 81-104.

Wacey, D., Menon, S., Green, L., Gerstmann, D., Kong, C., Mcloughlin, N., ... & Brasier, M. (2012). Taphonomy of very ancient microfossils from the∼ 3400 Ma Strelley Pool Formation and∼ 1900 Ma Gunflint Formation: New insights using a focused ion beam. *Precambrian Research*, *220*, 234-250.???

Webster, C. R., Mahaffy, P. R., Atreya, S. K., Flesch, G. J., Mischna, M. A., Meslin, P. Y., ... & Martín-Torres, J. (2015). Mars methane detection and variability at Gale crater. *Science*, *347*(6220), 415-417.
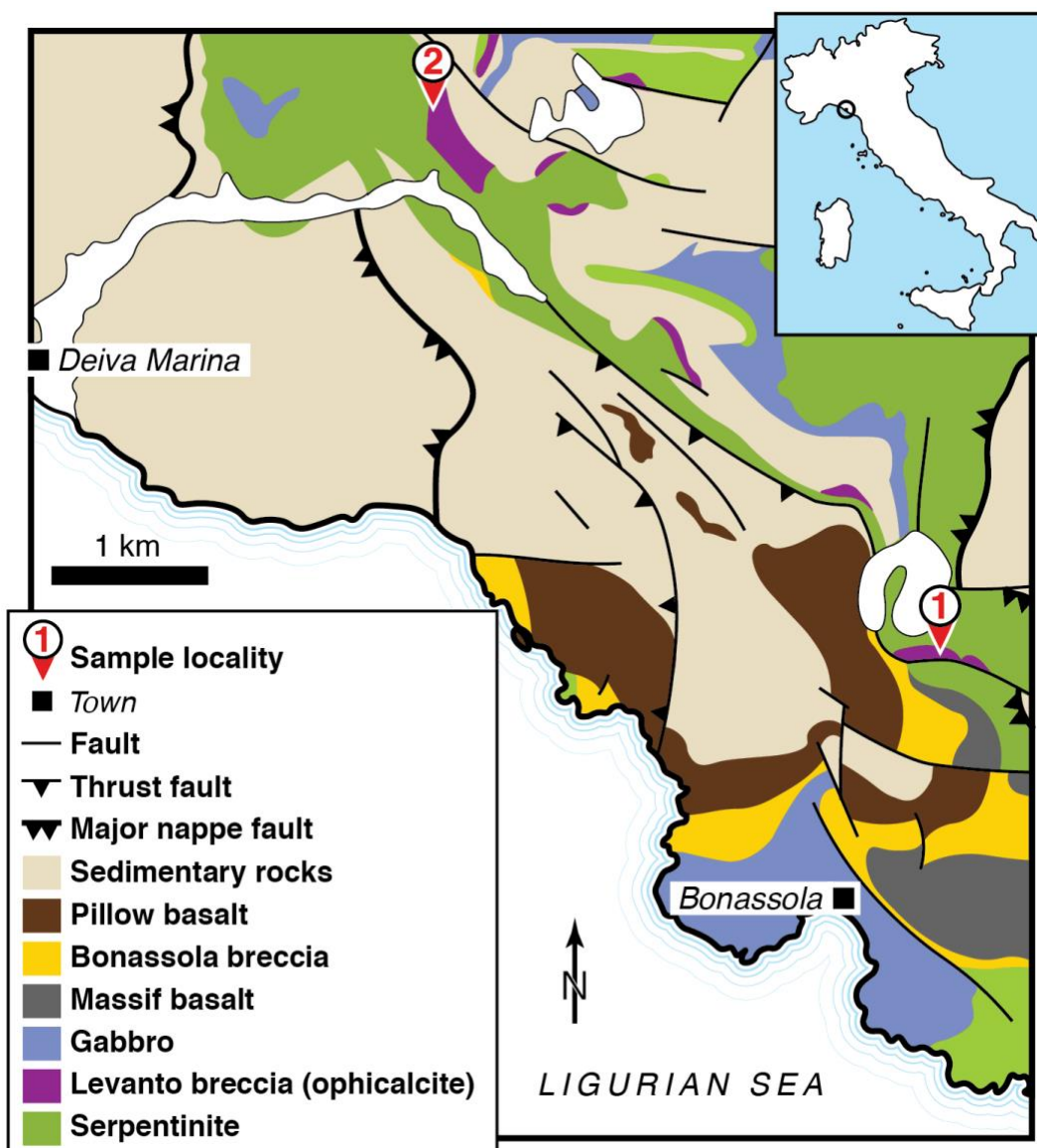
Figure Captions

Fig. 1. Geological map showing the localities of filament-bearing calcite vein samples collected inland from Bonassola (1) and Deiva Marina (2). Adapted from Strating & Wamel (1989).
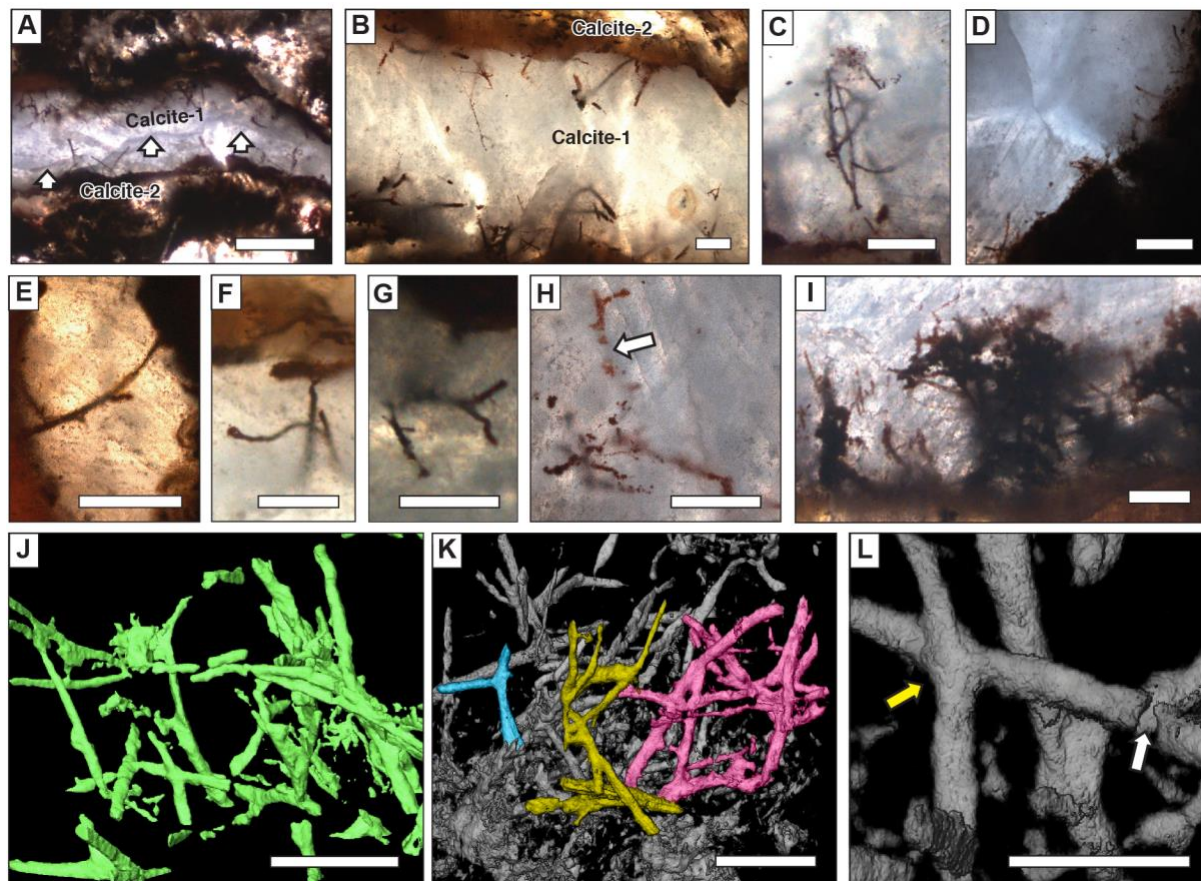
Fig 2. Photomicrographs (A–I) and synchrotron X-ray microtomography renderings (J–L) of filament assemblages in calcite veins. All photomicrographs were taken in plane-polarised, transmitted light. **(A)** Calcite vein with filaments from Locality 1, showing somewhat blocky calcite with irregular median suture (arrowed). **(B)** Opaque filaments clustering on both sides of Calcite-1 within a vein mantled by brown, fibrous Calcite-2 (Locality 1). **(C)** Curving, connected filaments (Locality 1). **(D)** Filaments from Locality 2. **(E)** A curved, possibly branched filament spanning the thickness of Calcite-1 (Locality 1). **(F)** A branching filament that swells towards the tip (Locality 1). **(G)** A branching filament (Locality 1). **(H)** Branching filaments with patchy preservation; arrow indicates gap (Locality 1). **(I):** An unusually dense population of filaments (Locality 1). **(J):** A three-dimensional view of the filaments in I showing curved trajectories; image is a cropped still frame from the supplementary movie. **(K)** An alternative view of the same region as I and J, showing numerous branches and interconnections; three contiguous regions are highlighted in colour. **(L)** Another view of the same region as I, J and K; white arrow indicates a conspicuous gap in one filament. This field of view shows an "X"-shaped pseudo-junction (yellow arrow) where filaments grazing each other are cemented together (and/or merged by the process of computing a surface through the rather diffuse filament margins). Some apparent connections seen in panel 2K may also result from these effects. **Scale bars:** 500 µm (A) 100 µm (B–I); 50 µm (J, K); 20 µm (L).
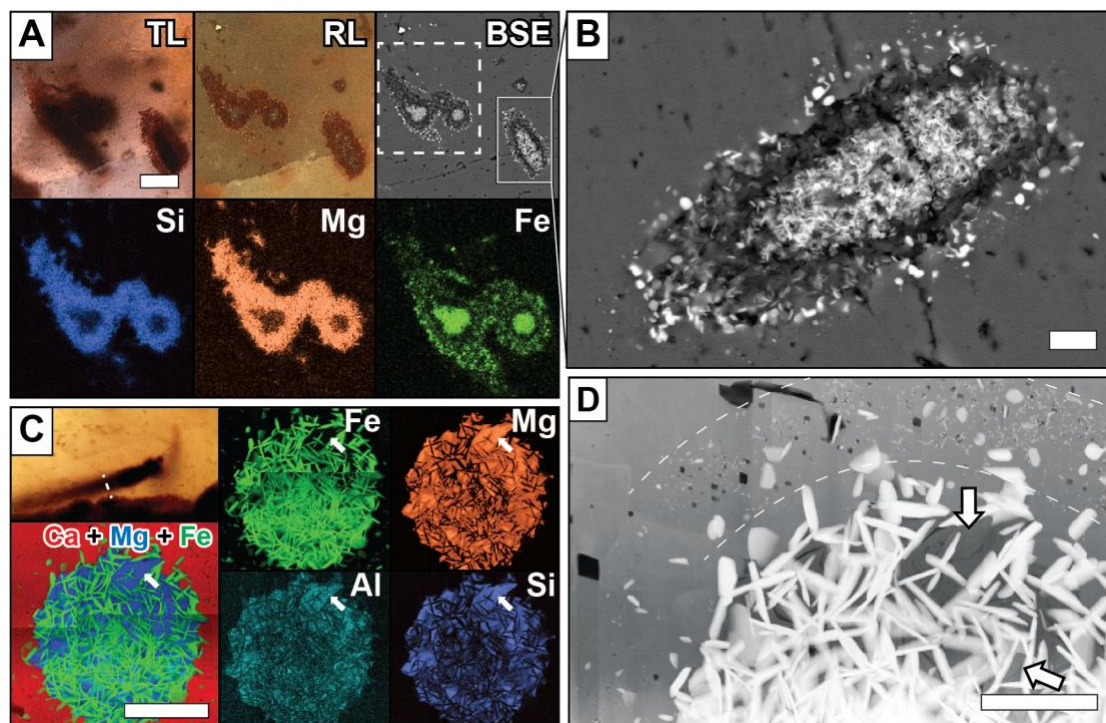
Fig 3. Optical and electron microscopy and energy-dispersive X-ray spectroscopy of filaments in calcite veins (Locality 1). (A) Thick filaments intersecting the surface of a polished thin section, imaged in transmitted light ("TL"), reflected light ("RL") and by means of backscattered electron microscopy ("BSE"), revealing a concentric structure that is typical of most filaments at both localities. Element maps obtained by energy-dispersive X-ray spectroscopy show the distribution of Fe (present as hematite), and Mg+Si (probably talc) within the filaments. Al is also slightly enriched in the Mg+Si phase (not shown). **(B)** Close-up of the BSE image in A, showing the slightly diffuse, microcrystalline nature of the filaments and their bimineralic structure. This filament is dissected obliquely by the thin section surface. **(C)** A filament subjected to FIB-milling to extract an ultrathin wafer, shown in transmitted light (with dashed line indicating line of FIB section) and in element maps obtained from the wafer. The distribution of Mg-silicate in this filament differs from those in A, but the element maps of Mg, Al, Si and Fe show that the first three of these elements are present in the same mineral while Fe occurs in a different mineral. Arrows indicate a prominent group of lath-shaped Al-bearing Mg-silicate crystals also visible in D. **(D)** A scanning transmission electron micrograph view of the filament shown in C. Arrows indicate lath-like Mg-silicate crystals, which show dark grey against the white platy hematite crystals. Dashed lines enclose a diffuse outer halo of hematite. **Scale bars:** 25 μm (A), 5 μm (B,C), 2.5 μm (D).
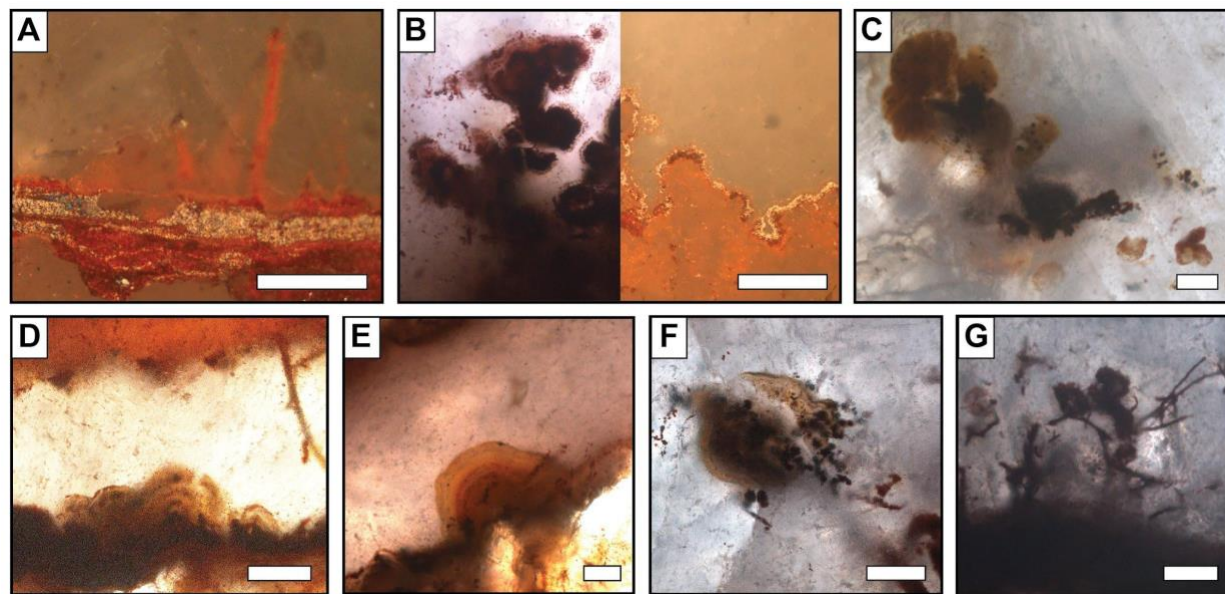
Figure 4: Photomicrographs of hematite + Mg-silicate microstructures. (A) Laminated cements lining the inner edge of Calcite-1, with attached red filaments (reflected light). **(B)** A ramifying growth structure somewhat similar to "Frutexites" in transmitted (left) and reflected (right) light; only the exterior of the structure appears to be laminated. **(C)** Globular, non-laminated growths (transmitted light). **(D)** Laminated domal growths (transmitted light). **€** Individual laminated dome (transmitted light). **(F)** Laminated irregular spheroid attached to filaments (transmitted light). **(G)** Blobs attached to filaments (transmitted light). **All scale bars 50 μm.**
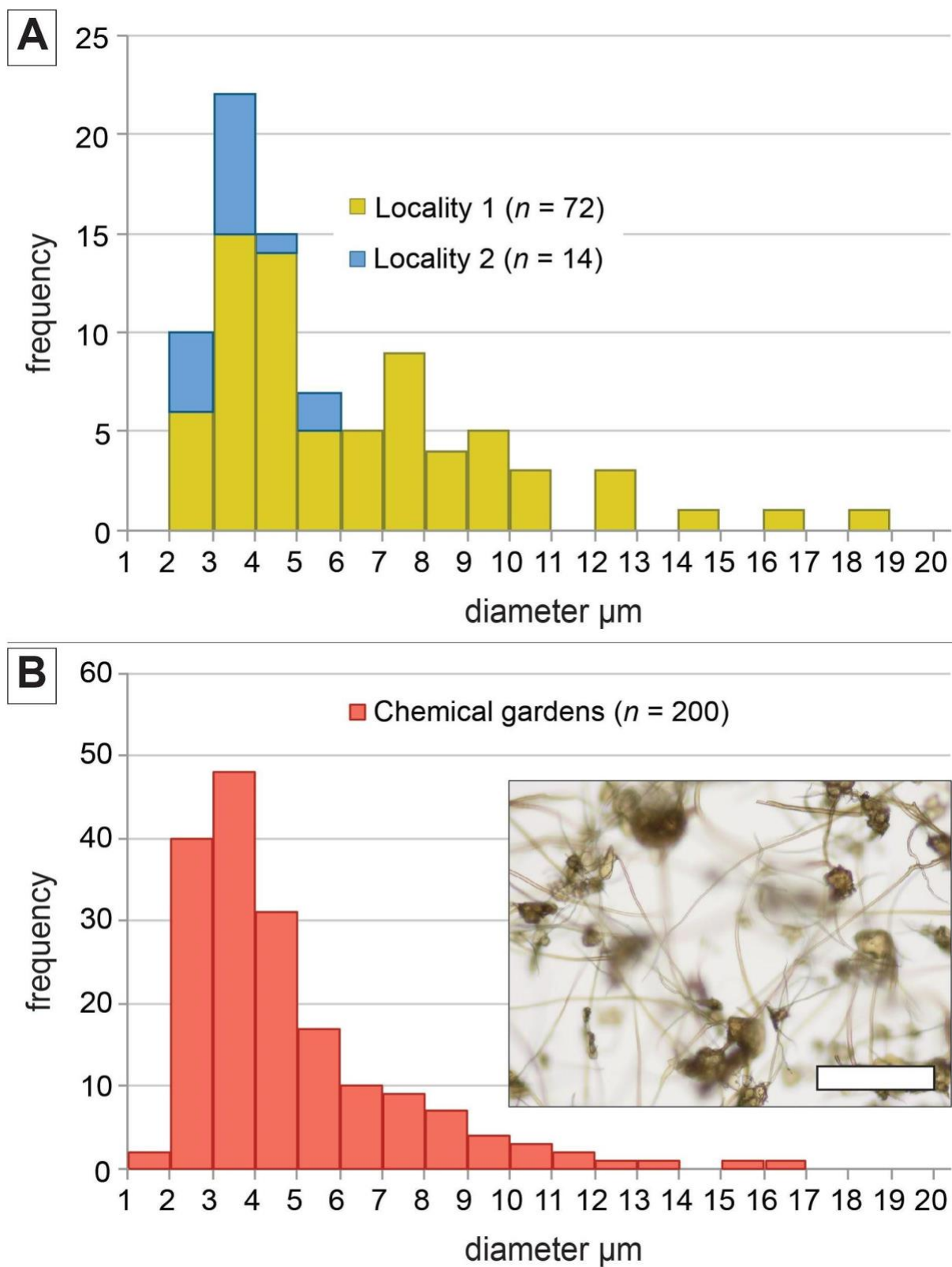
Figure 5: Histogram comparing diameters of Ligurian filaments and chemical gardens.
(A) Diameters of filaments in calcite veins were similar at two localities ~4 km apart (for map

positions see Figure 1). **(B)** Diameters of tubular filaments in abiotic chemical gardens produced by McMahon (2019) from seed particles <63 μm. Inset: photomicrograph of chemical garden filaments included in the population represented by the histogram. Scale bar: 200 μm.
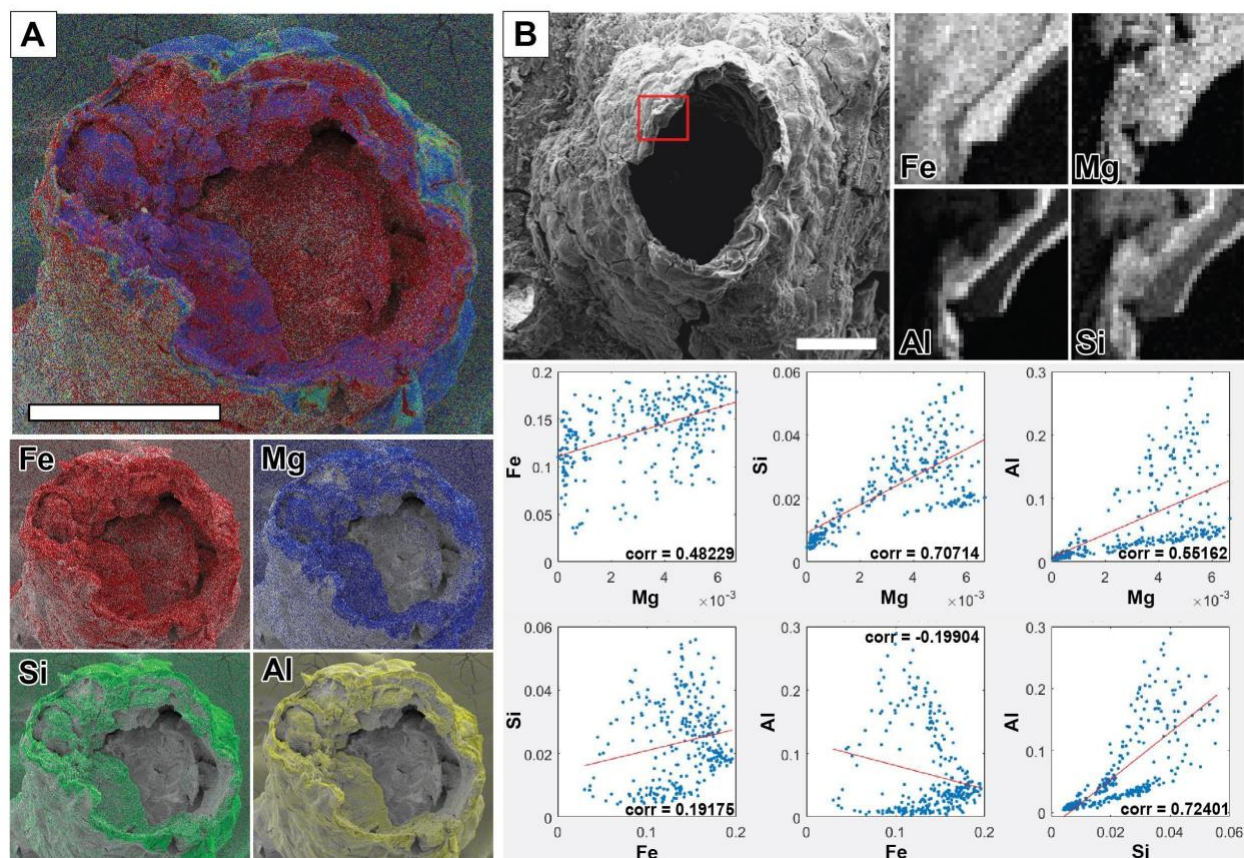

Figure 6: Element distributions in experimental chemical gardens produced from polymetallic seed salts. (A) EDS maps of Fe, Mg, Si and Al overlaid on SEM image of chemical garden tube. Note that the innermost precipitates are dominated by Fe, while Mg, Si and Al are present in layers in the wall. Scale bar = 250 μm. **(B) Associations between elements in a chemical garden tube wall.** Top-left: SEM image (scale-bar = 250 μm) of an experimental chemical garden tube; red box shows region of element maps (scale-bar = 25 μm). Note multi-layer structure different from that shown in Supplementary Fig. 3. Top right: coarsened, normalized element maps show the boxed region. These were used to calculate correlation coefficients; each pixel provides one point in the scatterplots, below.